NASA/TM—2018-219938 (Corrected Copy)

Overview and Evaluation of a Computational Bone Physiology Modeling Toolchain and Its Application to Testing of Exercise Countermeasures

Alexander Schepelmann and Christopher R. Werner
ZIN Technologies, Inc., Middleburg Heights, Ohio

James A. Pennline and Beth E. Lewandowski
Glenn Research Center, Cleveland, Ohio

Lealem Mulugeta
Universities Space Research Association, Houston, Texas

Corrected Copy issued June 2019.

August 2018

NASA STI Program . . . in Profile

Since its founding, NASA has been dedicated to the advancement of aeronautics and space science. The NASA Scientific and Technical Information (STI) Program plays a key part in helping NASA maintain this important role.

The NASA STI Program operates under the auspices of the Agency Chief Information Officer. It collects, organizes, provides for archiving, and disseminates NASA's STI. The NASA STI Program provides access to the NASA Technical Report Server—Registered (NTRS Reg) and NASA Technical Report Server—Public (NTRS) thus providing one of the largest collections of aeronautical and space science STI in the world. Results are published in both non-NASA channels and by NASA in the NASA STI Report Series, which includes the following report types:

- TECHNICAL PUBLICATION. Reports of completed research or a major significant phase of research that present the results of NASA programs and include extensive data or theoretical analysis. Includes compilations of significant scientific and technical data and information deemed to be of continuing reference value. NASA counter-part of peer-reviewed formal professional papers, but has less stringent limitations on manuscript length and extent of graphic presentations.

- TECHNICAL MEMORANDUM. Scientific and technical findings that are preliminary or of specialized interest, e.g., "quick-release" reports, working papers, and bibliographies that contain minimal annotation. Does not contain extensive analysis.

- CONTRACTOR REPORT. Scientific and technical findings by NASA-sponsored contractors and grantees.

- CONFERENCE PUBLICATION. Collected papers from scientific and technical conferences, symposia, seminars, or other meetings sponsored or co-sponsored by NASA.

- SPECIAL PUBLICATION. Scientific, technical, or historical information from NASA programs, projects, and missions, often concerned with subjects having substantial public interest.

- TECHNICAL TRANSLATION. English-language translations of foreign scientific and technical material pertinent to NASA's mission.

For more information about the NASA STI program, see the following:

- Access the NASA STI program home page at http://www.sti.nasa.gov

- E-mail your question to help@sti.nasa.gov

- Fax your question to the NASA STI Information Desk at 757-864-6500

- Telephone the NASA STI Information Desk at 757-864-9658

- Write to:
  NASA STI Program
  Mail Stop 148
  NASA Langley Research Center
  Hampton, VA 23681-2199

NASA/TM—2018-219938 (Corrected Copy)

Overview and Evaluation of a Computational Bone Physiology Modeling Toolchain and Its Application to Testing of Exercise Countermeasures

Alexander Schepelmann and Christopher R. Werner
ZIN Technologies, Inc., Middleburg Heights, Ohio

James A. Pennline and Beth E. Lewandowski
Glenn Research Center, Cleveland, Ohio

Lealem Mulugeta
Universities Space Research Association, Houston, Texas

Corrected Copy issued June 2019.

National Aeronautics and
Space Administration

Glenn Research Center
Cleveland, Ohio 44135

August 2018

Acknowledgments

The authors would like to thank Kelly M. Gilkey, Abhishektha Boppana, and Aaron P. Godfrey for their assistance with this research.

Level of Review: This material has been technically reviewed by technical management.

Available from

NASA STI Program
Mail Stop 148
NASA Langley Research Center
Hampton, VA 23681-2199

National Technical Information Service
5285 Port Royal Road
Springfield, VA 22161
703-605-6000

This report is available in electronic form at http://www.sti.nasa.gov/ and http://ntrs.nasa.gov/

Corrected Copy

Issued June 2019 for

NASA/TM—2018-219938
Overview and Evaluation of a Computational Bone Physiology Modeling Toolchain and Its Application to Testing of Exercise Countermeasures
Alexander Schepelmann, Christopher R. Werner, James A. Pennline, Beth E. Lewandowski, and Lealem Mulugeta
August 2018

The plots on pages 21, 22, 24, and 25 were updated to corrections in the cortical and trabecular results. Changes were made in the text within pages 21 to 25, to reflect the changes in the plots. Those changes appear in last paragraph, page 21; paragraph 1, page 22; last paragraph, page 23; end of section 5.2, page 24; and in the discussion of Figure 8, page 25.

Abstract

Prolonged microgravity exposure disrupts natural bone remodeling processes and can lead to a significant loss of bone strength, increasing injury risk during missions and placing astronauts at a greater risk of bone fracture later in life. Resistance-based exercise during missions is used to combat bone loss, but current exercise countermeasures do not completely mitigate the effects of microgravity. To address this concern, we present work to develop a personalizable, site-specific computational modeling toolchain of bone remodeling dynamics to understand and estimate changes in volumetric bone mineral density (BMD) in response to microgravity-induced bone unloading and in-flight exercise. The toolchain is evaluated against data collected from subjects in a 70-day bed rest study and is found to provide insight into the amount of exercise stimulus needed to minimize bone loss, quantitatively predicting post-study volumetric BMD of control subjects who did not perform exercise, and qualitatively predicting the effects of exercise. Results suggest that, with additional data, the toolchain could be improved to aid in developing customized in-flight exercise regimens and predict exercise effectiveness.

1 Introduction

Prolonged microgravity exposure during long-duration space missions can have detrimental effects on astronaut bone health (Zérath, 1998)(Vico et al., 2000)(Sibonga et al., 2007a). Weightlessness experienced by flight crews during extended spaceflight results in skeletal unloading, which disrupts natural bone remodeling processes experienced in a 1 g environment (van Loon et al., 1996, Chapter 5). This lack of mechanical stimulus on weight-bearing bone sites triggers bone resorption and can lead to a 0.4-2.7% loss of volumetric bone mineral density (BMD) per month, which lowers bone strength and increases in-flight injury risk (Keyak et al., 1994)(Lang et al., 2004)(Nelson et al., 2009). Furthermore, astronauts who returned from long-duration missions could take up to 9 months to restore 50% of lost bone, with full volumetric BMD and bone strength recovery not being observed 1 year after mission conclusion (Lang et al., 2006)(Sibonga et al., 2007b). Therefore spaceflight-induced bone loss perhaps permanently increases post-flight injury risk.

Performing resistance exercise during spaceflight can stimulate bone formation (Goodship et al., 1998)(Shackelford et al., 2004)(Orwoll et al., 2013). A comparative study by Smith et al. (2012) analyzed exercise and dietary data for 13 astronauts flying International Space Station (ISS) missions between 2006 and 2009. The authors showed that, in conjunction with an appropriate in-flight diet, individuals who performed adequately varied resistance exercise of sufficient magnitude returned from 4 to 6 month space missions without a significant change in bone mass and BMD compared to pre-flight values in most bone regions. Individuals who instead participated in an exercise regimen with less variation saw a decrease in both bone mass and BMD compared to pre-flight values, which demonstrates that subject-specific exercises, combined with personalized nutrition programs, can mitigate astronaut bone loss during long-duration missions.

To minimize astronaut risk in- and post-flight, NASA's Cross-Cutting Computational Modeling Project aims, in part, to create predictive models of bone strength that could be used to assess bone health and inform personalized exercise countermeasures for crew members on long-duration space missions (White and McPhee, 2007). Previous work investigated the creation of a computational model that combined existing knowledge of cellular and mechanotransduction dynamics to simulate the effects of microgravity on cortical and trabecular bone, to provide quantitative analysis of bone mass and calcium levels during spaceflight and post-mission recovery, and to probabilistically asses bone fracture risk (Pennline, 2009)(Chang and Pennline, 2013)(Sibonga et al., 2017)(Nelson et al., 2009). Subsequent work focused on incorporating finite element (FE) methods into this computational model with the intention to capture changes in BMD and elastic modulus resulting from in-mission exercises performed by astronauts on the ISS (Werner and Gorla, 2013)(Pennline and Mulugeta, 2014a). This paper builds on this work, and presents efforts to develop a personalizable, site-specific computational modeling toolchain of bone remodeling dynamics to understand and estimate changes in volumetric BMD in response to microgravity-induced bone unloading and in-flight exercise. In this toolchain, pre-flight bone densitometry scans are processed using a Gaussian Naïve Bayes (GNB) classifier to create personalized FE models of an astronaut's skeleton and to initialize a computational bone model that simulates bone dynamics at the bone remodeling level. The FE and computational models are then executed iteratively for the duration of simulated spaceflight to propagate model parameters. Virtual loads applied to the generated FE models simulate the effects of exercise and influence the modeled mechanotransduction dynamics by affecting the rate of bone remodeling.

The rest of the paper is organized as follows: In section 2 we present the procedure used to process pre-flight densitometry data and explain how this information is used to generate personalized FE bone models. In section 3, we summarize the computational model, specifically highlighting improvements over the bone remodeling model published by Pennline (2009) and Pennline and Mulugeta (2014a). In section 4, we present experiments to evaluate the toolchain's ability to predict trends of femur volumetric BMD using data collected from subjects in a 70-day bed rest study. Results of this evaluation are discussed in section 5. We find that the toolchain provides insight into the amount of exercise stimulus needed to minimize bone loss, and that it can create subject-specific bone models that are potentially useful for quantifying the amount of exercise stimulus needed to mitigate volumetric BMD decline during spaceflight. Specifically, the toolchain predicts post-study cortical volumetric BMD of control subjects who did not perform exercise with a relative error of $-0.61 \pm 3.53\%$, and post-study trabecular volumetric BMD with a relative error of $-9.43 \pm 11.00\%$. The toolchain also qualitatively predicts the effect of exercise in mitigating bone loss, showing that post-study volumetric BMD values can be achieved when non-zero forces are applied to the femur, though the magnitude of these forces is lower than expected. Likely reasons for these results are discussed. The paper concludes with a discussion of future work, summarizing how the toolchain could be improved and further validated with additional test data, as

well as how it could be used to develop customized in-flight exercise regimens and predict exercise effectiveness.

2 Finite element model generation

Bone models are procedurally generated by combining user-guided pre- and post processing steps with a probabilistic classification scheme to identify bone containing pixels in input bone densitometry scan data. This process allows a user to quickly generate subject-specific FE models that can be used in conjunction with the mechanotransduction model discussed in the next section to study the effects of exercise on volumetric BMD. This section details the FE model generation process in the context of a custom graphical-user-interface (GUI) based program developed for this task (Fig. 1). FE models are created from input data in four steps: user-guided pre-processing, probabilistic pixel classification, post processing, and FE model generation. These steps are described in the following subsections.

2.1 DICOM CT image stack pre-processing

Personalized FE models are generated from pre-flight Digital Imaging and Communications in Medicine computed tomography (DICOM CT) image stacks. For a specific subject, the generated FE model and corresponding bone densitometry data are used to initialize and propagate the computational bone remodeling model described section 3 when simulating exercise.

After loading DICOM CT data, scan contrast and sharpness can be adjusted to increase the intensity difference between bone- and non-bone containing pixels, as well as to remove noise from the image that could lead to misclassification (Fig. 1a). These changes are applied to the entire image stack and are modified using the sliders located beneath the plot of CT slices. Image contrast is modified for individual pixels using MATLAB's `imadjust()` Image Processing Toolbox function (The Mathworks, Inc., Natick, MA). This function maps grayscale values in the original image into a new range, whose lower or upper limit are defined by the "Contrast" GUI slider value, depending on whether the image is darkened or lightened. Darkening the image modifies the mapping's lower limit; lightening the image modifies the mapping's upper limit. Image sharpness is adjusted using MATLAB's `imsharpen()` Image Processing Toolbox function, which modifies local pixel neighborhoods using a Gaussian lowpass filter whose standard deviation is defined by the "Sharpness" GUI slider value.

Classification is performed on a user-specified image region of interest (ROI), whose size and position can be modified using buttons in the GUI. The classification can be further constrained by selecting groups of pixels within this ROI using a binary mask, whose lower and upper limit intensity threshold values can be adjusted by the user through the "Min Mask Thresh" and "Max Mask Thresh" sliders in the GUI. Pixels within this intensity range are then processed with a heuristic that first removes disconnected volumes using MATLAB's `bwareaopen()` Image Processing Toolbox function, followed by hole filling operations on each ROI slice using MATLAB's `imfill()` and `imclose()` Image Processing Toolbox functions. This results

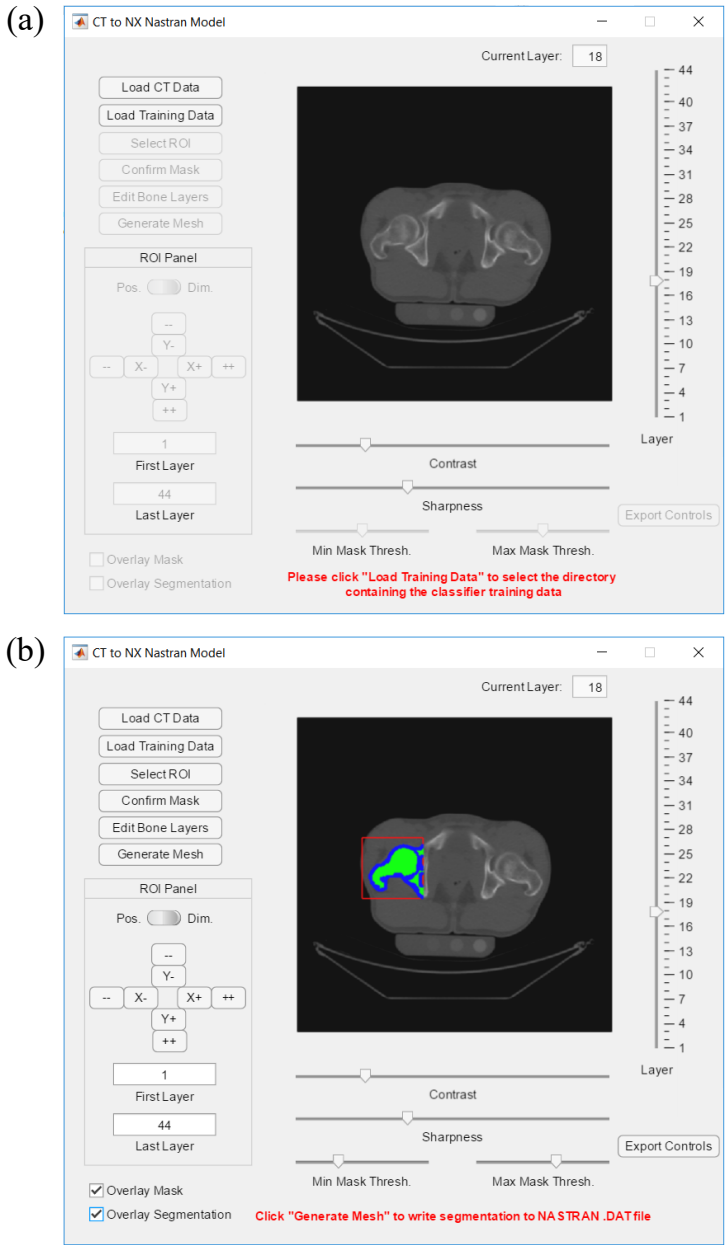

Figure 1.—FE generation GUI. (a) User-guided pre-processing. After loading a DICOM CT image stack, scan contrast and sharpness can be adjusted by the user to help the probabilistic classifier more easily distinguish between bone and non-bone pixels. The right slider can be used to scroll through each slice of the image stack. (b) Probabilistic classification results. Classification is performed on pixels in the user-specified ROI. After automated segmentation, user-guided post processing can be performed within the GUI prior to generating the mesh in order to isolate individual bones and correct misclassifications. Red: User-specified ROI. Blue: Identified cortical bone. Green: Identified trabecular bone.

in a binary mask that approximately captures the desired bone-containing region in the image, decreasing the amount of required post processing after classification.

2.2 Probabilistic scan segmentation

CT scan data is automatically segmented using a probabilistic classification scheme. This scheme assigns data in the DICOM image stack to one of three classes: cortical bone, trabecular bone, and non-bone. Automated processing algorithms have previously been used for segmentation tasks involving bone, as they reduce labor, time, and segmentation variability (Folkesson et al., 2007)(Malan et al., 2013). Specifically, data is categorized using a Naïve Bayes classifier whose likelihood of features are assumed to follow a normal distribution, a scheme colloquially known as GNB (John and Langley, 1995)(Mitchell, 1997). GNB classification is widely used for image labeling and segmentation tasks, including medical images (Wang and Summers, 2012). For completeness, we summarize this classification scheme below.

Bayes classifiers are a family of probabilistic classification schemes that use Bayes' theorem to determine what class $Y = y_j$ a sample most likely belongs to based on a vector of features $\mathbf{X} =< x_1, x_2, ..., x_n >= \mathbf{X_i}$ (Bishop, 2006). Bayes' theorem takes the form

$$P(Y = y_j|\mathbf{X} = \mathbf{X_i}) = \frac{P(\mathbf{X} = \mathbf{X_i}|Y = y_j)P(Y = y_j)}{P(\mathbf{X} = \mathbf{X_i})} \tag{1}$$

where $P(Y = y_j|\mathbf{X} = \mathbf{X_i})$ is the posterior probability that a sample Y belongs to class y_j given that the feature vector $\mathbf{X}$ is equal to $\mathbf{X_i}$, $P(\mathbf{X} = \mathbf{X_i}|Y = y_j)$ is the conditional probability that the feature vector $\mathbf{X} = \mathbf{X_i}$ was observed given that a sample Y belongs to class y_j, $P(Y = y_j)$ is the prior probability that a sample Y belongs to class y_j, and $P(\mathbf{X} = \mathbf{X_i})$ is the probability that a feature vector $\mathbf{X}$ equals $\mathbf{X_i}$.

In Naïve Bayes classification, each feature k in $\mathbf{X}$ is "naïvely" assumed to be conditionally independent of every other feature, meaning that the conditional probability model can be rewritten as a product of independent probabilities over every feature as

$$P(\mathbf{X} = \mathbf{X_i}|Y = y_j) = \prod_{k=1}^{n} P(\mathbf{X_i}(k) = x_k|Y = y_j) \tag{2}$$

where x_k is the specific value of the individual feature. The denominator in equation 1 is independent of the class label, and is therefore constant for all y_j. Since classification is only concerned with the relative likelihood that a sample belongs to a given class, it is therefore possible to calculate that a given input vector $\mathbf{X_i^{new}}$ most likely belongs to the class Y^{new} using the rule

$$Y^{new} \longleftarrow \arg\max_{y_j} P(Y = y_j) \prod_{k=1}^{n} P(\mathbf{X_i}(k) = x_k|Y = y_j) \tag{3}$$

Like its name suggests, a GNB classifier assumes that the likelihood of each feature in $\mathbf{X_i}$ follows a normal distribution, which is defined by feature k's mean

and variance for a given class, μ_c and σ_c^2, respectively. This allows the likelihood for each feature for each class to be calculated as

$$P(\mathbf{X_i}(k) = x_k | Y = y_j) = \frac{1}{\sqrt{2\pi\sigma_c^2}} exp\left(-\frac{(x_k - \mu_c)^2}{2\sigma_c^2}\right) \tag{4}$$

Labeled training data is required to calculate μ_c and σ_c^2. After transforming input data into the appropriate feature space, these quantities are calculated as

$$\mu_c = \frac{1}{m}\sum_{i=1}^{m} x_i \tag{5}$$

and

$$\sigma_c^2 = \frac{1}{m}\sum_{i=1}^{m} (x_i - \mu_c)^2 \tag{6}$$

where x_i are the individual feature values belonging to a given class, and m is the total number of feature values for a given class. Similarly to equation 5, the prior probability for each class can be calculated as the quotient between the number of samples belonging to class $Y = y_j$ and the total number of samples in all classes.

2.3 Post processing and model generation

After probabilistic classification, a post processing heuristic is applied to identified cortical and trabecular pixels. The heuristic ensures that cortical and trabecular locations are physiologically feasible, and that identified pixels will generate a continuous two-material FE model. A cortical outer boundary for pixels in each CT slice is first created by performing an image erosion on the binary mask generated in section 2.1 using MATLAB's `imerode()` Image Processing Toolbox function and subtracting it from the original mask. The pixels under the resulting mask are then added to the set of cortical labels identified via the probabilistic classification scheme described in section 2.2. Thereafter, trabecular labels are assigned to the remaining pixels in the interior of the original mask.

The resulting set of labeled pixels may contain misclassifications or multiple bones. To correct classification errors and isolate bones of interest, user-guided post processing can be performed within the GUI by clicking the "Edit Bone Layers" button. This launches a new window, where labeled pixels in the user-specified ROI can be reassigned to one of the three classes.

After post processing, a standalone NASTRAN (MSC Software, Newport Beach, CA) FE model, composed of six-sided solid element connection CHEXA elements, can be generated from the segmentation by clicking the "Generate Mesh" button. Model element spacing is extracted from metadata contained in the DICOM CT image stack. Material properties for each element are then calculated based on identified bone labels and corresponding pixel intensities of unadjusted images in the DICOM image stack using the following procedure: volumetric BMDs (ρ_{QCT}) for each element are first calculated from CT scan Hounsfield unit intensity values (H) as

$$\rho_{QCT} = \alpha H + \beta \tag{7}$$

where the coefficients α and β are calculated from a linear regression of calibration phantom densities present in the CT scan (Keyak et al., 1994). Due variability in intensity values resulting from scan parameters, regression coefficients should be recalculated for each CT scan (Giambini et al., 2014). Next, the mean ρ_{QCT} values for cortical ($\bar{\rho}_{QCT}^{cort}$) and trabecular ($\bar{\rho}_{QCT}^{trab}$) bone are calculated using the identified bone labels, which in turn are used to calculate a mean ash density ($\bar{\rho}_{ash}^{cort}$ and $\bar{\rho}_{ash}^{trab}$) for each type of bone as

$$\bar{\rho}_{ash}^{cort} = 0.887\bar{\rho}_{QCT}^{cort} + 0.0633 \tag{8}$$

$$\bar{\rho}_{ash}^{trab} = 0.887\bar{\rho}_{QCT}^{trab} + 0.0633 \tag{9}$$

where the constants were determined from load tests of human cadaveric proximal femora (Keyak et al., 2005). Corresponding mean elastic modulus values for cortical and trabecular bone ($\bar{E}^{cort}$ and $\bar{E}^{trab}$) are finally calculated as

$$\bar{E}^{cort} = 14900\bar{\rho}_{ash}^{cort1.86} \tag{10}$$

$$\bar{E}^{trab} = 14900\bar{\rho}_{ash}^{trab1.86} \tag{11}$$

with regression coefficients again calculated from load tests of cadaveric femora (Keyak et al., 2005). Mean shear moduli ($\bar{G}^{cort}$ and $\bar{G}^{trab}$) are calculated for each bone type as

$$\bar{G}^{cort} = \bar{E}^{cort}/(2(1+\nu)) \tag{12}$$

$$\bar{G}^{cort} = \bar{E}^{trab}/(2(1+\nu)) \tag{13}$$

assuming a Poisson's ratio of $\nu = 0.3$.

3 Computational bone remodeling model

The computational bone model simulates bone remodeling dynamics to capture changes in volumetric BMD in response to skeletal unloading with the goal of capturing bone loss trends in microgravity. Specifically, the model is designed to understand and estimate site-specific changes in volumetric BMD in response to skeletal unloading and exercise-induced skeletal loading, which in turn affects bone material properties and bone strength. Using long-duration bed rest as an analogue to microgravity, the generated FE models described in the previous section can be coupled with the bone remodeling model to predict cortical and trabecular volumetric BMD in the presence of skeletal unloading and resistive exercise performed in a 70-day bed rest study. This section summarizes the computational bone model, highlighting extensions of the model originally published by Pennline (2009) and Pennline and Mulugeta (2014a), and discusses how it is integrated with generated FE models to propagate model parameters and simulate the effects of exercise-induced skeletal loading.

3.1 Computational model

The computational model is designed to simulate changes in bone volume fraction (BVF) over time by modeling osteoblast and osteoclast cell dynamics, which form and resorb bone, respectively (Bronner and Worrell, 1999). Specifically, cellular dynamics equations developed for this model describe the bone remodeling process accomplished by groups of osteoblasts and osteoclasts working together in so-called bone remodeling units (BRUs). During this process, retired osteoblasts, called osteocytes, are permanently captured in bone, after which they are believed to function as the primary mechanosensors in bone structure (Bonewald, 2006). BRUs proceed through ordered stages of activation, resorption, reversal, and formation, followed by a quiescent stage (Parfitt, 1988). While osteoclast and osteoblast lineages each include distinct cell types exhibiting varying levels and requiring multiple steps of differentiation (Ott, 2010), the model developed here uses a simplified approximation. Cellular processes such as differentiation, apoptosis, bone formation, and bone resorption occur over several days or months (Eriksen, 2010), while biochemical concentrations tend to establish equilibrium on a much shorter timescale (Lemaire et al., 2004). Specifically, receptor-ligand binding reactions are assumed to occur much faster than respective changes in cell numbers (Pivonka et al., 2008). Therefore, we here assume quasi-steady-state binding of ligands to receptors and associated signaling events and effects leading to cell responses.

The net effect of the interaction between the osteoblast and osteoclast cells can be related to the change in BVF through the equation

$$\frac{dBVF}{dt} = A_f \bar{f}_a \frac{B(t)}{B_0} - A_r \bar{f}_a \frac{C(t)}{C_0} \tag{14}$$

where A_f is the area of bone formed per BRU in a cross section of a volume element, A_r is the area of bone removed per BRU in a cross section of a volume element, $\bar{f}_a$ is the activation density in a steady state expressed as number of BRUs activated per day per area, B is the population of osteoblasts, B_0 is a reference osteoblast population, C is the population of osteoclasts, and C_0 is a reference osteoclast population. In the developed model, equation 14 and the governing equations described below are identical for cortical and trabecular bone regions. Behavioral differences for both types of bone occur due to numerical differences of A_f and in the computation of $\bar{f}_a$, which is calculated based on formulas developed for each bone type (Hernandez et al., 1999). Physiologically, significant changes in BVF should increase or decrease $\bar{f}_a$. The model therefore assumes the instantaneous value of activation density f_a to be proportional to the fractional change in BVF relative to its initial value BVF_0

$$f_a = \frac{BVF(t)}{BVF_0} \bar{f}_a \tag{15}$$

and substitutes this expression into equation 14, yielding

$$\frac{dBVF}{dt} = A_f \frac{BVF(t)}{BVF_0} \bar{f}_a \frac{B(t)}{B_0} - A_r \frac{BVF(t)}{BVF_0} \bar{f}_a \frac{C(t)}{C_0} \tag{16}$$

Osteoid, the collagen matrix produced by osteoblasts, gradually mineralizes following formation, over a period that can vary from 6 months to 1 year (Parfitt,

1988). During and immediately after peak formation, a region of bone is therefore expected to exhibit a lower than usual degree of mineralization. The model considers bone volume as the sum of mineralized and osteoid volume. Therefore, BVF can be considered the sum of mineralized volume fraction M and osteoid volume fraction O

$$BVF = M + O \tag{17}$$

The model relates BVF, M, O, and volumetric BMD using the relationship developed by Pennline and Mulugeta (2017). With this method, the initial values BVF_0, M_0, and O_0 are calculated from initial volumetric BMD values extracted from input CT image stacks as explained in section 2. By respectively modeling the rate of formation r_f and rate of resorption r_r as $A_f \cdot f_a$ and $A_r \cdot f_a$, the differential equations governing osteoid and mineralized BVFs can be written as

$$\frac{dO}{dt} = r_f \frac{B}{B_0} - r_r \frac{C}{C_0} \left(\frac{O}{O+M} \right) - r_m O \tag{18}$$

$$\frac{dM}{dt} = r_m O - r_r \frac{C}{C_0} \left(\frac{M}{O+M} \right) \tag{19}$$

where r_m is the bone mineralization rate. This rate can be obtained through the initial values BVF_0, M_0, and O_0 and applying steady-state conditions to equations 18 and 19, yielding the relationship

$$r_m O_0 = r_r \left(\frac{M_0}{O_0 + M_0} \right) \tag{20}$$

The cellular dynamics equations model rates of change of active osteoclasts, active osteoblasts, and committed precursors of active osteoblasts called responding osteoblasts (B_r) as a set of coupled differential equations. Equations in this model are adapted from Lemaire et al. (2004) and can be written as

$$\frac{dB_r}{dt} = D_{B_P} E_{TGF} - D_{B_r}((1 - E_{TGF}) + E_{PGE}) B_r \tag{21}$$

$$\frac{dB}{dt} = ((1 - E_{TGF}) + E_{PGE}) D_{B_r} B_r - (1 - E_{PTH}) A_B B \tag{22}$$

$$\frac{dC}{dt} = E_{RL} D_{C_P} - E_{TGF} A_C C \tag{23}$$

where variables represent the following quantities: D_{B_P} is the differentiation rate of osteoblast progenitors, D_{B_R} is the differentiation rate of responding osteoblasts, D_{C_P} is the differentiation rate of osteoclast progenitors, E_{TGF} is the $TGF - \beta_1$ receptor occupancy ratio, E_{PGE} is prostaglandin PGE_2 receptor occupancy, E_{PTH} is parathyroid hormone receptor occupancy, E_{RL} is the RANKL receptor occupancy ratio, A_B is the rate of elimination of B, and A_C is the rate of elimination of C (apoptosis). Initial values of B_0 and C_0 are obtained by solving the steady-state case of the nonlinear system; in these equations the expression for E_{TGF} allows the system to be uncoupled. This three variable model is a specific case of one of two

general mathematical models that have been identified as capable of describing the process of bone remodeling (Zumsande et al., 2011).

The above model extends the work by Lemaire et al. (2004) by adding two mediators, PGE_2 and nitric oxide (NO), which contribute to balance between resorption and formation via cell expression in response to skeletal loading. This receptor-ligand interaction can cause cell proliferation while other interactions simultaneously inhibit proliferation dynamics. For example, the factor $(1 - E_{PTH})$ in equation 22, which is not present in Lemaire et al. (2004), has been introduced here to comply with experimental evidence that PTH exhibits an inhibitory effect on the apoptosis of active osteoblasts (Jilka et al., 1999)—as E_{PTH} increases, apoptosis of B decreases. The basic biological assumption is that cell proliferation is proportional to receptor occupancy. The model assumes that the biochemical concentrations establish equilibrium immediately, relative to the much slower timescale at which cellular populations evolve. The steady-state or equilibrium value is obtained by equating the appropriate governing differential equation to zero under the assumption that the current cellular populations are fixed. Receptor occupancy ratios, a real number between 0 and 1, represent the proportion of ligand receptors that are occupied. The remainder of this section details the derivation for terms in equations 21 to 23, concluding with an explanation of how they relate to skeletal loading experienced during exercise.

3.1.1 Parathyroid Hormone

Ignoring osteoblastic interactions, the interaction of PTH with its receptor is regarded as an ordinary chemical reaction according to

$$\mathrm{P} + \mathrm{P}_r \underset{\mathrm{k_6}}{\overset{\mathrm{k_5}}{\rightleftharpoons}} \mathrm{P}_r \cdot \mathrm{P} \tag{24}$$

where P (pM) is the concentration of unbound PTH, P_r (pM) is the concentration of unoccupied PTH receptors, $P_r \cdot P$ (pM) is the concentration of the complex between PTH and its receptor, and k_5 (1/pM/day) and k_6 (1/day) are the rates of the forward and reversion reactions, respectively. Assuming the law of mass action, we deduce from the reaction above a system equivalent to that provided by Lemaire et al. (2004), but with slightly different notation:

$$\frac{dP}{dt} = S_p + I_p + k_6 P_r \cdot P - k_5 P(P_r^T - P_r \cdot P) - k_p P \tag{25}$$

$$\frac{dP_r \cdot P}{dt} = k_5 P(P_r^T - P_r \cdot P) - k_6 P_r \cdot P \tag{26}$$

Here, $P_r^T = P_r + P_r \cdot P$ is the total concentration of PTH receptors that are fixed and determined by current cellular populations of B and B_R, S_p and I_p (pM/day) are the basal rate of synthesis and the injection rate of PTH, respectively, and k_p (1/day) is the relative rate of decay of PTH. At equilibrium, the receptor occupancy ratio of PTH is given by

$$E_{PTH} = \frac{P_r \cdot P}{P_r^T} = \frac{S_p + I_p}{S_p + I_p + k_p \frac{k_6}{k_5}} \tag{27}$$

3.1.2 RANK/RANKL/OPG pathway

The treatment of the RANK/RANKL/OPG pathway is a variation on the model of Lemaire et al. (2004) with the addition of the effects of NO. The interactions between RANK (K), RANKL (L), OPG ($\mathcal{O}$), the RANK-RANKL complex ($K \cdot L$) and the OPG-RANKL complex ($\mathcal{O} \cdot L$) can be summarized by

$$\mathcal{O} + L \underset{\mathrm{k_2}}{\overset{\mathrm{k_1}}{\rightleftharpoons}} \mathcal{O} \cdot L \tag{28}$$

$$K + L \underset{\mathrm{k_4}}{\overset{\mathrm{k_3}}{\rightleftharpoons}} K \cdot L \tag{29}$$

This leads to the system

$$\frac{d\mathcal{O}}{dt} = p_{\mathcal{O}} - k_1 \mathcal{O} L + k_2 \mathcal{O} \cdot L - d_{\mathcal{O}} \tag{30}$$

$$\frac{d\mathcal{O} \cdot L}{dt} = k_1 \mathcal{O} L - k_2 \mathcal{O} \cdot L \tag{31}$$

$$\frac{dL}{dt} = p_L - k_1 \mathcal{O} L + k_2 \mathcal{O} \cdot L - k_3 K L + k_4 K \cdot L - d_L \tag{32}$$

$$\frac{dK \cdot L}{dt} = k_3 K L - k_4 K \cdot L \tag{33}$$

Following the original work, the concentration K of RANK is assumed to be a fixed constant. The variations that come into play are the alternative expression for the anti-proliferative effect of a ligand receptor complex and the effects of NO (using the Hill function derived in section 3.1.4) on the production and degradation rates of OPG and RANKL. For OPG, the production rate $p_{\mathcal{O}}$ and degradation rate $d_{\mathcal{O}}$ are proposed as

$$p_{\mathcal{O}} = r_{\mathcal{O}} B (1 - E_{PTH}) E_{NO} + I_{\mathcal{O}} \tag{34}$$

$$d_{\mathcal{O}} = k_{\mathcal{O}} \mathcal{O} \tag{35}$$

where $r_{\mathcal{O}}$ (1/day/cal) is the maximum rate of production of OPG per active osteoblast, E_{NO} is the Hill function describing the intensity of the effects of NO (sect. 3.1.4), $I_{\mathcal{O}}$ (pM/day) is the rate of injection of OPG, and $k_{\mathcal{O}}$ (1/day) is the relative decay of OPG. This yields the formula

$$\mathcal{O} = \frac{r_{\mathcal{O}}}{k_{\mathcal{O}}} B (1 - E_{PTH}) E_{NO} + \frac{I_{\mathcal{O}}}{k_{\mathcal{O}}} \tag{36}$$

The way the factor E_{NO} is used is motivated by the experimental results of (Fan et al., 2004), in which it is suggested that NO stimulates the production of OPG and inhibits the production of RANKL by affecting transcription. So with regard to RANKL, the production rate p_L and degradation rate d_L can be given by

$$p_L = r_L B_r \left(1 - \frac{L + \mathcal{O} \cdot L + K \cdot L}{N_L R}\right) E_{PTH} (1 - E_{NO}) + I_L \tag{37}$$

$$d_L = k_L L \tag{38}$$

where r_L (1/day/cell) is the maximum rate of production of RANKL per responding osteoblast, I_L (pM/day) is the rate of injection of RANKL, N_L is the maximum number of RANKL molecules that can be attached to the surface of each responding osteoblast, and k_L (1/day) is the relative decay rate of RANKL. Note that the expressions in equations 37 and 38 are different from those of Lemaire et al. (2004). Changes to these equations include interchanging the roles of B and B_R as suggested by Pivonka et al. (2008), as well as the inclusion of the inhibitory effect of NO on the production of RANKL. In the pseudo-steady state, this results in the following RANKL concentration and RANK receptor occupancy ratio:

$$L = \frac{r_L B_r E_{PTH}(1 - E_{NO}) + I_L}{(1 + \frac{k_1}{k_2}\mathcal{O} + \frac{k_3}{k_4}K)\frac{r_L}{N_L}E_{PTH}(1 - E_{NO}) + k_L} \tag{39}$$

$$E_{RL} = \frac{K \cdot L}{K} = \frac{k_3}{k_4}L \tag{40}$$

3.1.3 Transforming Growth Factor Beta ($TGF - \beta_1$)

Of the three isoforms of $TGF - \beta$, $TGF - \beta_1$ is the most abundant isoform, being one of two of the largest sources, and is the isoform involved in the bone remodeling process (Janssens et al., 2005). As a ligand, the binding with its receptor, treated as a chemical reaction, follows the analysis for PTH and its receptor and leads to the occupancy ratio given by

$$E_{TGF} = \frac{S_T}{S_T + k_T\frac{k_8}{k_7}} = \frac{\frac{S_T}{k_T}}{\frac{S_T}{k_T} + \frac{k_8}{k_7}} = \frac{T}{T + \frac{k_8}{k_7}} \approx \frac{T}{T + 15.8} \tag{41}$$

where T is the concentration of unbound TGF-β_1, S_T (pM/day) is the rate of synthesis of TGF-β_1, k_T is the degradation rate (1/day), and k_7 and k_8 are the rates of the forward and reverse reactions, respectively. Trabecular receptors also have the highest affinity for TGF-β_1 with a dissociation constant (k_8/k_7) of 15.8±7.6 pmol/l (Tripathi et al., 1993).

In the model, the primary source of available TGF-β_1 is assumed to be released during the resorption phase of the bone remodeling process (Roodman, 1999). As a result, TGF-β_1 concentration is modeled as

$$S_T = T_B \rho_t r_r \frac{C}{C_0} \cdot 10^3 \tag{42}$$

where T_B (pmol/g)is the concentration of TGF-β_1 stored in bone tissue, ρ_t (g/cc) is the true density of bone (Hernandez et al., 2001), and $r_r C/C_0$ is the rate at which bone is resorbed divided by the total volume of the domain. In order for T to represent the average daily concentration, k_T is set to 1. The expression for TGF-β_1 concentration presented in equation 42 is significant for two reasons. First, the equation closely connects cell dynamics to resorption and formation rates presented in equation 14. Second, it allows steady-state values of B_0, C_0, and B_{r0} to be solved for directly, as this term allows the cellular system of equations to decouple.

3.1.4 Nitric Oxide (NO)

NO, as well as PGE_2, play an anabolic role in bone remodeling. Although NO is not a ligand, an effector expression that acts in a similar way to how a receptor occupancy ratio acts in the system of equations fits the cell proliferation/anti-proliferation assumption. To begin, the model assumes the following differential equation to describe the concentration of NO (N):

$$\frac{dN}{dt} = S_N - d_N N \tag{43}$$

where S_N defines the rate of cell expression of NO according to the level of bone apposition or resorption suggested by the daily strain ϵ in Frost's Mechanostat Theory and d_N (1/day) is the relative degradation rate. S_N is given by

$$S_N = p_N f_s(\epsilon) Y_d BVF \tag{44}$$

where p_N is the rate per cell, $f_s(\epsilon)$ is a functional relationship that mathematically describes the apposition or resorption of bone in response to the effect of daily strain resulting from exercise-induced bone loading, and Y_d is the osteocyte density. Combining equations 43 and 44 and assuming a pseudo-steady-state of $dN/dt = 0$ yields

$$N = \frac{p_n f_s(\epsilon) Y_d BVF}{d_N} \tag{45}$$

In one experimental study, the dose-dependent effects of NO on RANKL protein levels appear to follow an approximate log-linear relationship (Fan et al., 2004). To capture this, the model uses a Hill function E_{NO}, which behaves similar to an occupancy ratio:

$$E_{NO} = \frac{N}{N + N_0(\frac{1}{\beta} - 1)} = \frac{f_s(\epsilon)(\frac{BVF}{BVF_0})}{f_s(\epsilon)(\frac{BVF}{BVF_0}) + (\frac{1}{\beta} - 1)} \tag{46}$$

where N_0 is the equilibrium coefficient of NO at $\epsilon = \epsilon_0$ and BVF=BVF_0. By construction, $0 \leq E_{NO} \leq 1$ and $\beta \in (0, 1)$ is the equilibrium value of E_{NO}. By equating a factor of 10 or 10^2 increase in N to a drop in RANKL protein level from 80% to 40% as seen in Fan et al. (2004), leads to rough estimates of β=$\frac{1}{5}$ or β=$\frac{1}{4}$. Experiments in this model assume a value of $\beta = 1/5$.

3.1.5 Prostaglandin E2 (PGE_2)

Conducting a similar analysis to the one performed for PTH and its receptor leads to a PGE_2 occupancy ratio of

$$E_{PGE} = \frac{S_G}{S_G + k_G \frac{k_{10}}{k_9}} \tag{47}$$

where k_9 (1/pM/day) and k_{10} (1/day) are the rates of the forward and reverse ligand-receptor reaction, k_G (1/day) is the rate of decay of PGE_2 and S_G/k_G is the

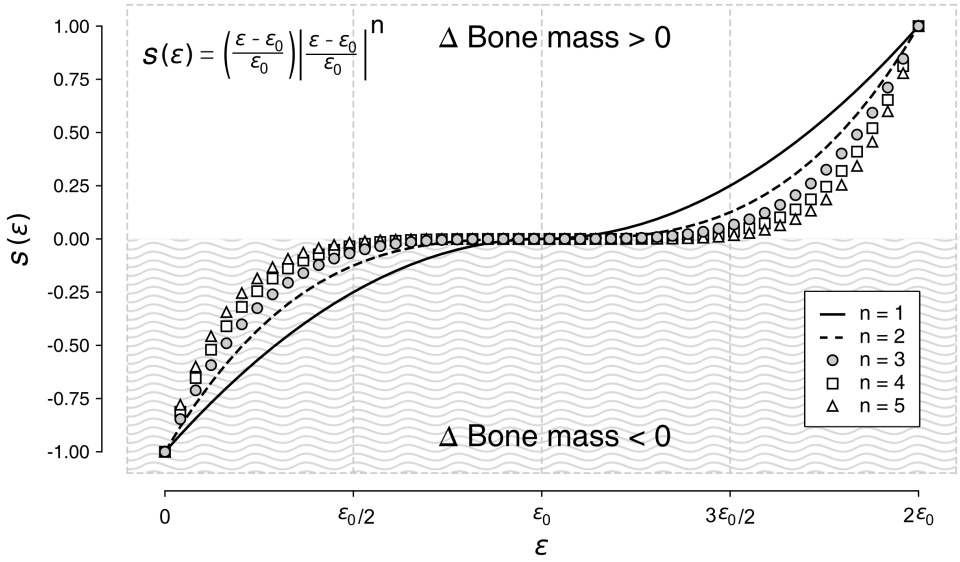

Figure 2.—Functional relationship s between the mechanical strain ϵ and bone apposition-resorption dynamics described by Frost's mechanostat theory.

concentration of PGE_2. Similarly to the synthesis rate for NO, the synthesis rate for PGE_2 is given by

$$S_G = p_G f_s(\epsilon) Y_d BVF \tag{48}$$

where p_G is the rate of PGE_2 per cell and Y_d is the osteocyte density. Dividing the numerator and denominator of equation 47 by $p_G Y_d BVF_0$ leads to

$$E_{PGE} = \frac{f_s(\epsilon) BVF/BVF_0}{f_s(\epsilon) BVF/BVF_0 + G_d} \tag{49}$$

where

$$G_d = \frac{k_G k_{10}}{p_G k_9 Y_d BVF_0} \tag{50}$$

The extent of binding of PGE_2 human plasma proteins was found to be 73% Raz (1972). If this value is used as the reference equilibrium value of E_{PGE} then $G_d = (1 - 0.73)/0.73$.

3.1.6 Daily mechanical strain

Exercise-induced bone stresses σ generate strain ϵ in bones in accordance with Hooke's Law (Hooke, 1678). Mathematically, this relationship can be written as

$$\sigma = E\epsilon \tag{51}$$

where E is the bone's elastic modulus. Aggregate daily strain resulting from exercise can be mathematically related to the apposition or resorption of bone via Frost's mechanostat theory (Frost, 2003) through the equation

$$f_s(\epsilon) = \left[\frac{\epsilon - \epsilon_0}{\epsilon_0} \left| \frac{\epsilon - \epsilon_0}{\epsilon_0} \right|^n + 1 \right] \tag{52}$$

where ϵ_0 represents the center of the mechanical usage window where there is physiological remodeling balance and n is a parameter which can be used to adjust the width of the apposition-resorption curve (Fig. 2). Note that in complete unloading there is no strain, i.e., $\epsilon = f_s(\epsilon) = 0$. In remodeling balance, $\epsilon \approx \epsilon_0$ and $f_s(\epsilon) = 1$. In general, if ϵ is in the disuse mechanical usage window, it follows that $f_s(\epsilon) < 1$, and the BVF rate of change is negative. If ϵ is within the mechanical remodeling balance window, it follows that $f_s(\epsilon) \approx 1$, and the rate of BVF change is zero. If ϵ is in the overload mechanical usage window, $f_s(\epsilon) > 1$, and the BVF rate of change is positive. The response from the daily strain shows its effect in the remodeling equations through the receptor occupancy ratio of PGE_2 and NO, as outlined in sections 3.1.4 and 3.1.5.

3.2 Finite element integration

The finite element model generated via the process described in section 2 is integrated with the computational bone remodeling model discussed in section 3.1 to simulate exercise-induced bone loading. Specifically, finite element analysis (FEA) is used to calculate exercise-induced bone stresses based on applied forces that result from various exercises throughout the simulation in order to update cortical and trabecular modulus values and propagate remodeling model parameters.

At the beginning of the simulation, a linear static FEA is conducted in FEMAP with NX NASTRAN 11.30 (Siemens Product Lifecycle Management Software Inc., Plano, TX) to calculate initial average cortical and trabecular von Mises stresses ($\bar{\sigma_j}$) based on exercise-specific force values, subject-specific body weight, subject-specific bone elastic moduli, and subject-specific bone shear moduli. The finite element simulation is executed programmatically from MATLAB using the FEMAP API compiled for Python in conjunction with a custom script written in Python 3 (Python Software Foundation, Beaverton, OR) that loads the finite element model, assigns material properties, initializes forces and constraints on user-specified model nodes, executes the FEA, and returns corresponding cortical and trabecular stress values after the analysis completes.

After calculating single-cycle-induced stresses for each prescribed exercise, the computational model described in section 3.1 then executes for a user-specified interval that discretizes the total study duration, using the subject-specific parameters and FEA calculated exercise-specific stresses as input. Based on the single-cycle stresses experienced during each exercise, the model then calculates an equivalent set of stresses for the total exercise regimen using a formula for the Daily Load Stimulus (DLS), a relationship which quantifies the mechanoadaptive response of bones based on mechanical stimulus experienced by bone tissue (Carter et al., 1987)(Whalen et al., 1988). The DLS equivalent stress is calculated using a modified relationship from an expression suggested by Turner and Robling (2003)

$$S = \sum_{j=1}^{k} ln(1 + N_j)\bar{\sigma_j} f_j \tag{53}$$

where S is the equivalent stress, N is the number of loading cycles per loading condition or number of repetitions per exercise j, and f_j is the frequency of repetitions for

each exercise. Compared to other expressions for DLS (Carter et al., 1987)(Hazelwood et al., 2001)(Hazelwood and Castillo, 2007)(Genc et al., 2009)(Cavanagh et al., 2010), this formulation was found to best capture characteristics of cyclic loading in terms of stress- and strain-like quantities at specific bone sites (Pennline and Mulugeta, 2014b). The equivalent stress and elastic modulus for each bone type is then used to update cortical and trabecular strains via Hooke's Law (Gere, 2004), which in turn updates remodeling model parameters and cortical and trabecular elastic moduli during the next iteration.

To account for effects of changing elastic moduli on exercise-induced stresses, FEA is used to recalculate single-cycle stresses and in turn update DLS equivalent stresses and strains at simulation times defined by the user-specified discretization interval. Exercise-specific forces and FE model geometry are assumed to be constant throughout the simulation.

4 Methods

The computational bone physiology modeling toolchain was evaluated using data collected from a 70-day head-down-tilt bed rest study (Taibbi et al., 2016). Bed rest studies act as an analog for spaceflight, here providing quantitative data about subject anthropometry, pre-study volumetric BMD, and post-study volumetric BMD under experimental conditions where exercise type, frequency, and duration is strictly controlled (LeBlanc et al., 2007)(Cromwell, 2012).

Subject-specific CT scans were not available in the data set used for analysis. As a result, a representative, two-material FE model was constructed from pre-study CT scan data using the procedure described in section 2, which was collected from a subject who participated in a 17-week bed rest study (LeBlanc et al., 2007). The scan contained no observable anomalies to adversely impact the toolchain evaluation results. Due to limitations of available data, the same scan was used to train the classifier and probabilistically generate the FE model in order to evaluate the functionality of the toolchain. Five features were used by the GNB classifier to segment the image after its sharpness and intensity were manually adjusted during the scan pre-processing step: pixel color, pixel color after each image slice was blurred using a two-dimensional (2D) Gaussian filter, edge intensity, edge intensity after each image slice was blurred using a 2D Gaussian filter, and the local standard deviation at each pixel in the image slice, calculated from a 3x3 neighborhood centered on the corresponding pixel. The Gaussian filter used to blur each image slice was created using MATLAB's `fspecial('Gaussian')` Image Processing Toolbox function. Edges were computed using a Sobel filter using MATLAB's default values and MATLAB's `imgradient()` Image Processing Toolbox function. Local standard deviation of each pixel was calculated using MATLAB's `stdfilt()` Image Processing Toolbox function. Mean and variance values for each trained feature were calculated from hand-labeled data, which was automatically adjusted to match user-specified pre-processing settings before training. After segmentation, labels were manually post processed to correct false classifications using the GUI before generating the FE model.

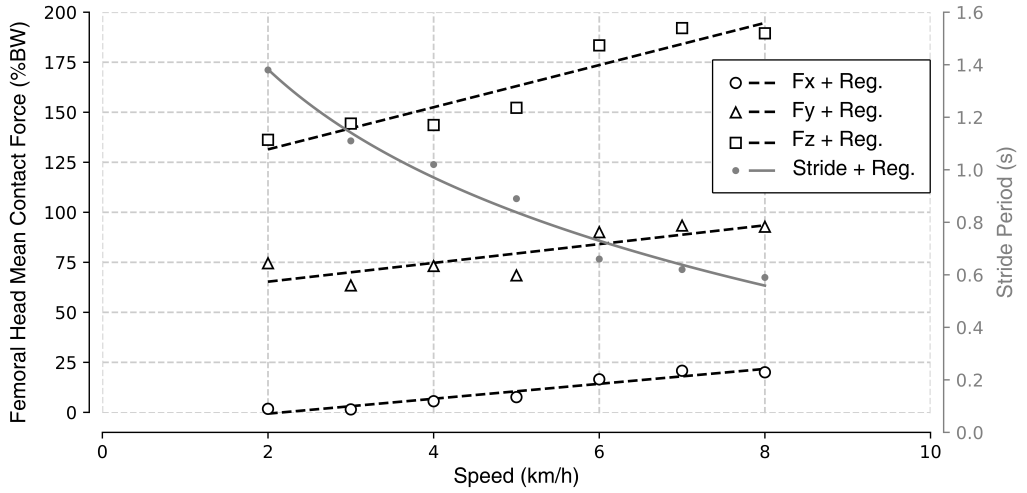

Figure 3.—Cartesian femoral head force and stride period regressions as a function of walking speed. Regression calculated for a single subject in the Orthoload database.

Bed rest study data contained usably complete measurement sets for 27 subjects. Of these, 7 subjects comprised the control group and did not perform exercise throughout the duration of the study; 20 subjects performed exercises that simulated NASA's integrated resistance and aerobic training (iRAT) study, which consisted of regularly scheduled high intensity interval-type aerobic exercises, continuous aerobic exercise, and resistance exercise (Cromwell, 2013)(Ploutz-Snyder et al., 2014).

Control group data was used to asses the computational bone remodeling model's ability to predict post-flight BMD values when subjects performed no exercise. Subject-specific cortical volumetric BMD, trabecular volumetric BMD, and mass were used to initialize the model, after which the model was executed to simulate 70 days of unloading. Model-predicted cortical and trabecular volumetric BMD values were compared to subject-specific cortical and trabecular volumetric BMD values measured at the end of the 70-day study.

Data from the remaining subjects was used to assess the computational bone remodeling model's ability to predict post-flight BMD values when subjects performed exercise. NASA's iRAT study is designed to maintain cortical and trabecular volumetric BMD during spaceflight. Due to modeling complexity, the net effect of this protocol was modeled as a single DLS exercise needed to maintain bone health—a walking exercise equivalent to taking 5,000 steps per day at a speed of 5 km/h, the approximate number of steps taken by adults in the United States at the average adult walking speed (Bassett et al., 2010)(Dean et al., 2001). In order to apply subject-specific forces to the FE model's femoral head ($\mathbf{F_{FH}}$), a regression was constructed from publicly available force data of a subject in the Orthoload database (Bergman, 2008), which yielded the following relationship between subject-specific mass (m), walking speed (v), and resulting Cartesian forces ($F_{x,FH}$, $F_{y,FH}$, $F_{z,FH}$) (Fig. 3):

$$\mathbf{F_{FH}} =< F_{x,FH}, F_{y,FH}, F_{z,FH} > \tag{54}$$

$$F_{x,FH} = m(0.4606v + 5.4868) \tag{55}$$

$$F_{y,FH} = m(0.0610v + 0.7265) = 0.1324F_{x,FH} \tag{56}$$

$$F_{z,FH} = m(0.9457v + 114.8431) = 2.053F_{x,FH} \tag{57}$$

Subject-specific muscle forces exerted on the greater trochanter during this exercise were modeled based on data published by Hazelwood and Castillo (2007), who report that during the stance phase of marathon running, the joint contact force at the femoral head is 2317N, and the muscle force on the greater trochanter is 1685N. The ratio of these forces was used to calculate subject-specific greater trochanter forces ($F_{x,GT}$, $F_{y,GT}$, $F_{z,GT}$) based on corresponding femoral head force components as

$$F_{x,GT} = (1685/2317)F_{x,FH} \tag{58}$$

$$F_{y,GT} = (1685/2317)F_{y,FH} \tag{59}$$

$$F_{z,GT} = (1685/2317)F_{z,FH} \tag{60}$$

Mean cortical and trabecular subject-specific stresses that result from applying these loads to the femur were calculated using the FEA procedure described in section 3.2. These stresses were used to calculate the corresponding DLS using a variant of equation 53, which additionally considers subject-specific stride period (Fig. 3) (Mulugeta and Pennline, in preparation).

Since pre- and post-study subject volumetric BMD values were known, but workouts performed by each subject were modeled as a lumped DLS exercise, optimization was used to assess the model's ability to predict the effects of the iRAT regimen by comparing the magnitude of DLS predicted forces in equations 55 to 60 with forces found via optimization. Specifically, the required force magnitude $F_{x,FH}$, which in turn defines all other force components on the femur, was optimized using the Covariance Matrix Adaptation Evolution Strategy (CMA–ES), a stochastic, derivative-free optimization algorithm (Hansen, 2006), in order to achieve post-study cortical and trabecular volumetric BMD values ($\bar{\rho}^{cort}_{QCT,meas}(\texttt{end})$ and $\bar{\rho}^{cort}_{QCT,meas}(\texttt{end})$) of exercising subjects. The optimization minimized the cost function

$$\begin{aligned} J(F_{x,FH}) = \gamma(\bar{\rho}^{cort}_{QCT,sim}(\texttt{end}) - \bar{\rho}^{cort}_{QCT,meas}(\texttt{end}))^2 + \\ (1-\gamma)(\bar{\rho}^{trab}_{QCT,sim}(\texttt{end}) - \bar{\rho}^{trab}_{QCT,meas}(\texttt{end}))^2 \end{aligned} \tag{61}$$

where $J(F_{x,FH})$ is the cost of the current evaluation, $\bar{\rho}^{cort}_{QCT,sim}(\texttt{end})$ and $\bar{\rho}^{cort}_{QCT,sim}(\texttt{end})$ are the simulated cortical and trabecular volumetric BMD values at the end of 70 days, γ is a weighting factor equal to the ratio of cortical pixels to total pixels in the generated FE model, and values of $F_{x,FH}$ were constrained to the range [0,∞). For each subject, the model was initialized using the corresponding pre-study cortical volumetric BMD, trabecular volumetric BMD, and subject mass. Cortical and trabecular volumetric BMD values were used to calculate elastic and shear modulus values for each subject using equations 8 to 13 and applied to the representative FE model. Forces were applied to the femoral head and greater trochanter at predefined nodes in the representative finite element model per the method described in

section 3. For computational efficiency, FEA to update stresses and modulus values was performed three times during the simulated 70-day study duration: once at the beginning of the simulation, as well as on day 23 (1/3 of the study duration) and on day 46 (2/3 of the study duration). The model's predictive ability was assessed by comparing optimized $F_{x,FH}$ values to the theoretical subject-specific maintenance force in equation 55.

5 Results and discussion

Work presented in this paper aims to create a personalizable, site-specific computational modeling toolchain of bone remodeling dynamics to understand and estimate changes in volumetric BMD in response to microgravity-induced bone unloading and in-flight exercise. This is accomplished by first building a subject-specific finite element model from input CT scan data using a probabilistic classification scheme, and then using it in conjunction with FEA and a computational bone model to predict the effects of exercise on volumetric BMD. Data from a 70-day bed rest study was used to evaluate the functionality of the developed toolchain. Conducted experiments specifically investigated the probabilistic classifier's ability to generate finite element models from CT data, as well as the computational bone model's ability to predict post-study volumetric BMD when used in conjunction with FEA. Results from these experiments are discussed in the following sections.

5.1 Probabilistic scan classification

The probabilistic classification scheme presented in section 2 is able to successfully generate two-material FE models using CT image stacks as input. The resulting FE model was composed of 22,565 cortical elements and 44,828 trabecular elements. Compared to the method described by Chang and Pennline (2013), which relies exclusively on user-defined pixel intensity thresholds to classify bone types, the proposed method generates FE models without any intrabone gaps. Indeed, comparing the FE model generated with the proposed method (probabilistic classification and minimal GUI-based post processing), to a model generated from the manually segmented CT image stack used to train the probabilistic classifier, reveals that the two models are identical (Fig. 4). Furthermore, FE models generated using the proposed scheme exhibit greater numerical stability during FEA than models generated using the method proposed by Chang and Pennline (2013), because they do not contain voxels with artificially low or high modulus values. Since cortical and trabecular material properties are calculated from the mean intensity value of all pixels belonging to each class, the proposed method is also less sensitive to noise and compression artifacts in the scan. While these results suggest that the proposed method along with its current features and feature values are capable of generating highly accurate two-material FE models from CT image stacks, it should again be noted that due to lack of available CT data, the same image stack was used for training and testing the probabilistic classifier in the initial automated segmentation step. This makes the training examples highly relevant to the test set and likely artificially boosts the initial probabilistic classification accuracy. While this does

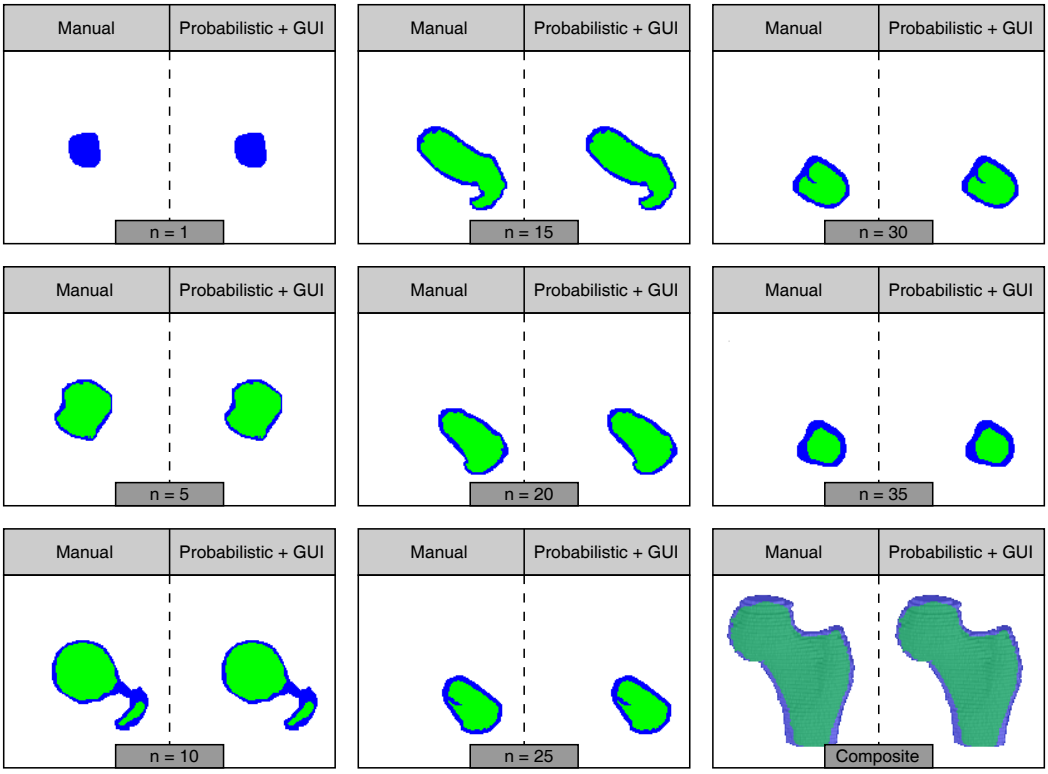

Figure 4.—Comparison between segmented CT image stacks at various layers n: manual vs. proposed method. The proposed method is able to produce an identical segmentation, resulting in an identical FEA model (lower right). Blue: Identified cortical bone. Green: Identified trabecular bone.

not affect the toolchain's ability to generate highly accurate FE models from CT images, since misclassified pixels can be corrected via manual post processing before generating the FE model, more data, if and when available, should be used to train the classifier to make it more robust to scan variability and decrease the potential amount of required post processing when trying to classify new CT images.

5.2 Toolchain predictive ability

The computational model has the capability to predict post-study cortical and trabecular volumetric BMD of control subjects who did not perform exercise with a mean percent error (MPE) of $-0.61 \pm 3.53\%$ and $-9.43 \pm 11.00\%$, respectively (Fig. 5). Compared to cortical values, predicted trabecular values exhibit a large MPE. This likely results from the sensitivity of trabecular bone volumetric BMD to remodeling rate values used in the model. Mean measured pre-versus-post cortical bone volumetric BMD of control subjects has a standard deviation of $\pm 3.45\%$ over the course of the study. Mean measured pre-versus-post trabecular bone volumetric BMD has a standard deviation of $\pm 11.87\%$ over the course of the study. Due to lack of available data, a single set of remodeling parameter values informed by literature

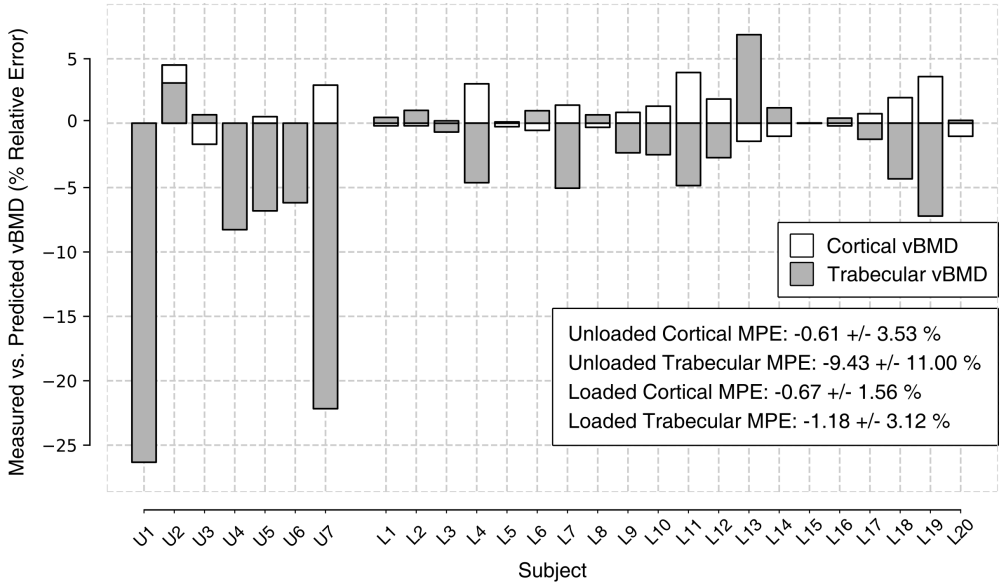

Figure 5.—Mean percent error between measured and predicted post-study cortical and trabecular volumetric BMD values using the proposed bone modeling toolchain. Post-study predicted volumetric BMD of loaded exercising subjects extracted result from force optimization trials. U: Unloaded control subject. L: Loaded exercising subject.

were used for all subjects, thereby not accounting for potentially important factors such as age, gender, and subject-specific anthropometry (Riggs et al., 2004) (Naganathan and Sambrook, 2003) (Kim et al., 2012). It is also likely that the width of the mechanostat deadzone window scales based on subject-specific values, but a single width was used for all trials. Furthermore, some model parameters, most notably the concentration of TGF-β_1 in equation 42 which was used to initialize and propagate the state variables of the computational bone model, may need to be varied to more accurately represent underlying physiology. Based on data published by Janssens et al. (2005), the model was evaluated with a TGF-β_1 concentration of 200μg/kg. However, other average concentrations have been observed by others (Hering et al., 2010). Moreover, wide variations depending on age and gender have been measured (Pfeilschifter et al., 1998). With additional volumetric BMD data, this work could be extended to investigate the relationship between these rates and factors, allowing us to further personalize the model on a subject-specific basis.

The optimization procedure described in section 4 is able to find subject-specific femoral head forces that lead model-predicted cortical and trabecular volumetric BMD values to converge on measured post-study values for all subjects (Fig. 5). Compared to measured values, model-predicted cortical values exhibit a MPE of $-0.67 \pm 1.56\%$ and trabecular values exhibit a MPE of $-1.18 \pm 3.12\%$. Furthermore, all forces found by the optimization are greater than zero, indicating that the proposed method qualitatively captures the benefits of exercise for maintaining

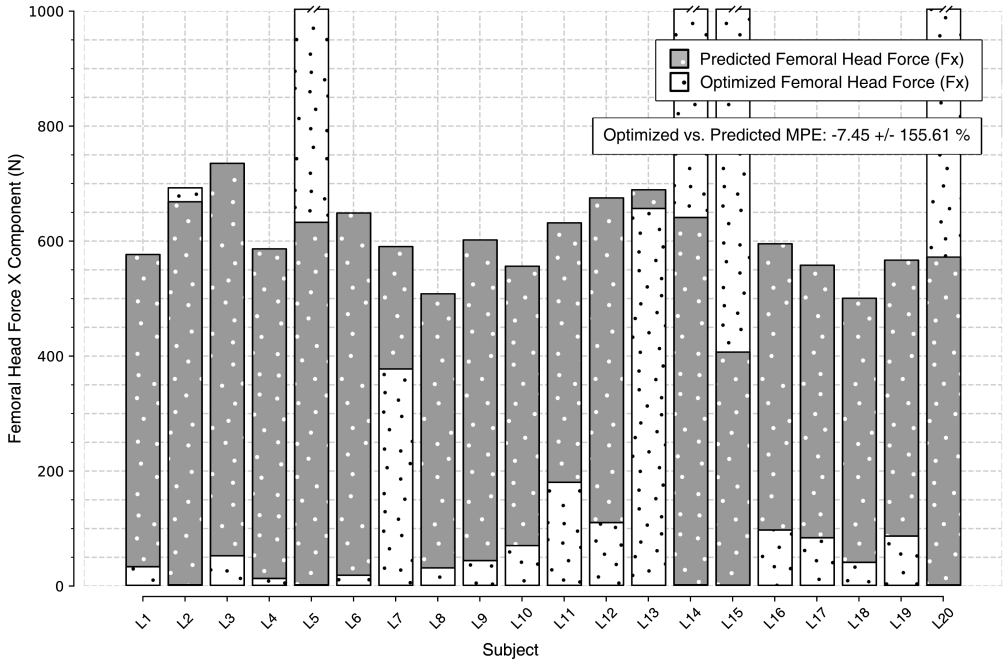

Figure 6.—Regression-predicted vs. optimized femoral head forces for exercising subjects.

volumetric BMD (Fig. 6). These results demonstrate the functionality of the computational bone model in conjunction with FEA and suggests that the toolchain accurately models bone remodeling dynamics, thus making it potentially useful for predicting volumetric BMD during extended bed rest and spaceflight. While the optimization is able to find a single force value that leads model-predicted values to converge on measured values, most of the identified forces are much lower than regression-predicted forces required for volumetric BMD maintenance for all but five test subjects. Optimized forces for four of these five subjects converged to physiologically unrealistic values of 1899.89 ± 391.31 N. Optimized forces exhibit a MPE of $-7.45 \pm 155.61\%$ compared to regression-predicted femoral head forces, indicating that additional work is necessary to further develop the model into a generalizable tool for quantitatively predicting the effects of specific exercises on volumetric BMD. In addition to evaluating the toolchain with only a single representative finite element model and parameter set for all subjects as described above, this error may result from several sources.

First, subject-specific regression-predicted forces may be artificially high. Femoral head forces used to create the regression were based on data collected from a single subject with an instrumented hip implant. It is not clear if ground reaction forces and gait patterns exhibited by this subject are representative of forces and patterns exhibited by the general population. Additional data needs to be incorporated into the regression in the future. While additional subject data is present in the OrthoLoad database, a regression that incorporates this data is not presented here

since optimizations were initialized using single-subject regression predicted femoral head forces. Initializing the optimization with a different force may lead the routine to converge on a different local minimum, making force comparisons between the performed optimization and regression predicted forces inappropriate.

Second, while interacting through the FE model during loading analysis, cortical and trabecular volumetric BMD are essentially separate quantities that evolve independently in the computational model. The cost function in equation 61 that is used to optimize BMD values considers cortical and trabecular values separately. As such, it is possible that the optimization converged on a local minimum that caused either cortical or trabecular value to be preferred, thus biasing the identified femoral head force. Comparing the MPE of cortical and trabecular volumetric BMD between measured and optimized values (Fig. 5) reveals that the relative error between the two quantities is not equal in several cases. While achieving a roughly equal error between these two quantities does not guarantee that the optimized force will be closer to the regression predicted force (e.g., subjects L8 and L16) (Fig. 6), the optimized femoral head force would be different had the optimization found a different minimum. Further work is needed to find a suitable costs function that is appropriate for optimizing femoral head forces. A potential way to mitigate the effects of optimizing these quantities independently would be to couple cortical and trabecular values directly by mapping them into a single quantity. This could be achieved by relating cortical or trabecular volumetric BMD and dual-energy X-ray absorptiometry (DXA) values via regression. Work in this area is ongoing.

Finally, systematic error may exist in the data. CT-derived bone density and corresponding material properties in the dataset used to evaluate the toolchain seem to be artificially low compared to other values found in literature (Hernandez et al., 2001)(Keyak et al., 2005). To investigate the impact of optimized forces in the presence of higher volumetric BMD, scaling factors were applied to cortical and trabecular volumetric BMD values in the evaluation dataset, which were calculated from published cortical and trabecular ash fraction BMD values collected for a study that investigated the relationship between quantitative CT scan data and bone mechanical properties (Kaneko et al., 2003)(Kaneko et al., 2004). Applying this scaling factor to the data resulted in cortical and trabecular volumetric BMD values that were 2.3 and 1.3 times higher, respectively. Forces were re-optimized using scaled values. These optimization results exhibit several interesting characteristics (Fig. 7).

First, optimization-found forces for scaled BMD values are higher, in aggregate, compared to optimization-found forces for unscaled BMD values. Disregarding trials for which both scaled and unscaled optimizations converged to physiologically unrealistic values (subjects L5, L14, L15, and L20), scaled optimization forces exhibit a mean percent change of $50.10 \pm 60.55\%$. This increase is interesting, as the absolute difference between starting and ending cortical and trabecular volumetric BMD is larger, meaning a larger drop in volumetric BMD, and therefore suggesting that a smaller maintenance force, should be found by the optimization. Conversely, it is also possible that sustaining a larger magnitude volumetric BMD requires a larger magnitude force. Work to investigate this phenomenon is ongoing. Consistent with this increase in force, scaling volumetric BMD did not cause the optimization to find

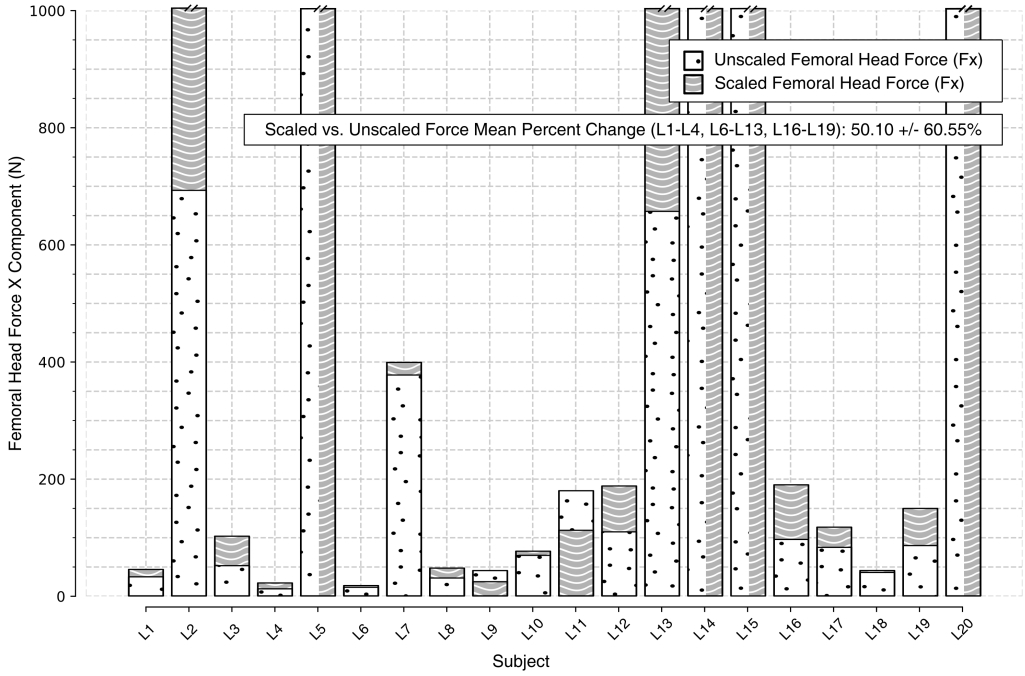

Figure 7.—Optimized femoral head forces for exercising subjects using scaled and unscaled volumetric BMD values.

physiologically realistic force values for subjects whose unscaled volumetric BMD values also failed to converge.

Indeed, scaling volumetric BMD values seems to destabilize the optimization, as forces for two additional subjects did not converge to physiologically realistic force values. This suggests that the parameters of the computational bone model need to be correspondingly adjusted when used with numerically larger cortical and trabecular volumetric BMD. This behavior may also result from the fact that cortical and trabecular volumetric BMD values are not scaled equally, therefore increasing the relative difference between these quantities, and thus making it more difficult for the optimization to converge using unadjusted computational bone remodeling model parameters. While forces for all but two of the remaining subjects increased when using scaled volumetric BMD values in the optimization, again suggesting that maintaining a higher BMD requires a higher load, it is unclear if these results are valid without being able to discount the effect of using unscaled bone remodeling parameters in the optimization. Further data is needed to investigate relationships between cortical and trabecular volumetric BMD values and bone remodeling model parameters to draw conclusions from this set of optimization results.

5.3 Effect of FEA-based parameter reinitialization

FEA is computationally expensive. In cases where optimization is used to determine the force required to maintain volumetric BMD, it is therefore preferable to perform

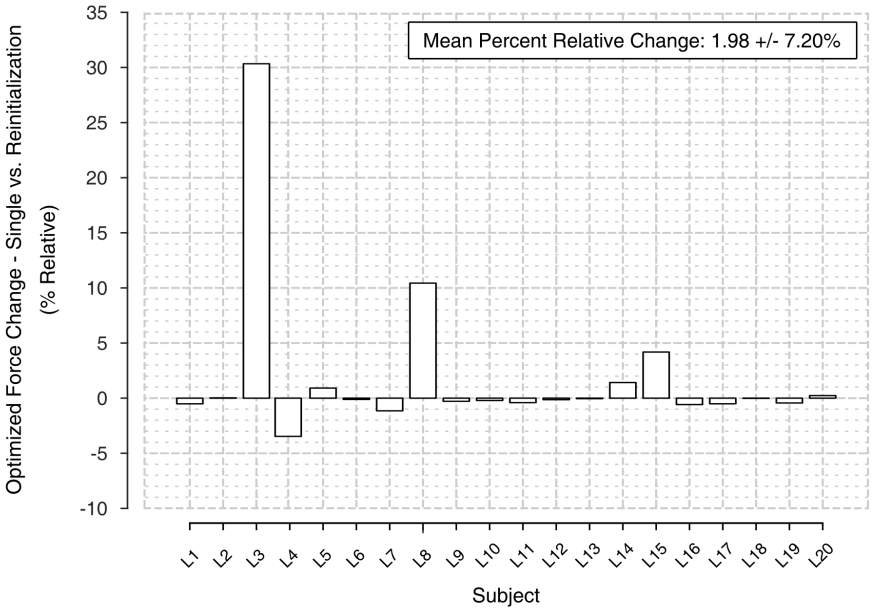

Figure 8.—Percent relative change in optimization-found forces when initializing exercise-related parameters only at the beginning of the 70-day study duration and reinitializing parameters at 1/3 and 2/3 of the 70-day study duration.

FEA as little as possible. In the previous experiments, exercise-related model parameters were recalculated throughout the study duration in order to account for changing elastic modulus values in the presence of bone unloading, but it is unclear what impact this reinitialization has on the magnitude of optimization-found forces needed to maintain BMD. To investigate the effect of parameter reinitialization, a final round of optimizations were performed that only calculated stress and modulus values at the beginning of the study period. The percent change between optimization predicted forces with and without parameter reinitialization are shown in figure 8. In 18 out of 20 cases, both optimizations find forces required to maintain volumetric BMD that differ from each other by less than 5%. In 2 out of 20 cases (L3 and L8), the relative percent change between forces found by the optimizations is greater than 10%. Examining these cases more closely suggests that this difference is likely a numerical artifact that results from the optimization-found forces being small. While the percent change of the optimization-found forces for these two subjects is relatively large compared to the percent changes observed in the other subjects, the resulting effect on the cortical and trabecular volumetric BMDs is small, resulting in cortical and trabecular volumetric BMD changes of less than 0.75%. Without these two subjects, the mean percent relative change between the optimization-found forces is $-0.06 \pm 1.44\%$. This suggests that parameter reinitialization is not necessary when using the tool to predict required maintenance forces for short-duration spaceflight. Further analysis and data are necessary to determine the effect of parameter reinitialization for longer duration missions.

6 Conclusion

Prolonged microgravity exposure disrupts natural bone remodeling processes and can lead to a significant loss of bone strength. Resistance-based exercise during missions can be used to combat bone loss, but currently employed countermeasures are general purpose and do not completely mitigate the effects of microgravity. To address this shortcoming, work in this paper detailed the development and evaluation of a personalizable computational modeling toolchain of bone remodeling dynamics, which aims to better predict changes in volumetric bone mineral density (BMD) in response to microgravity-induced bone unloading and in-flight exercise.

The toolchain is able to create accurate, personalized finite element models from input computed tomography (CT) data using a probabilistic classification scheme. The resulting classification requires minimal post processing and, compared to previous methods, decreases the time needed to create individualized models that exhibit greater numerical stability during finite element analysis (FEA).

The presented computational bone model is able to quantitatively predict respective cortical and trabecular volumetric BMD of control subjects with mean percent errors (MPEs) of $-0.61 \pm 3.53\%$ and $-9.43 \pm 11.00\%$ after 70 days of bed rest during which the subjects did not perform exercise. Qualitatively, in conjunction with FEA, the toolchain also predicts the mitigating effects of exercise for other subjects involved in the 70-day study by finding that non-zero forces lead to volumetric BMD maintenance, making it potentially useful for creating personalized predictions of bone strength during long-duration spaceflight and evaluating the efficacy of in-flight exercises in mitigating bone loss. However the magnitude of forces needed to maintain pre-study values is lower than expected.

The toolchain is eventually intended to be useful in designing personalized exercise regimens for flight crews on long-duration missions. To do this, work on this model needs to be expanded with additional data to account for the effects of subject-specific bone geometry and resulting exercise-induced stresses during FEA, as well as the effects of gender, age, and body anthropometry on bone remodeling rates in the computational model. Further research also needs to be conducted to be able to model specific exercises in terms of a Daily Load Stimulus.

With available data, immediate work can be performed to determine the effects of the cost function used for force optimizations, which treated cortical and trabecular volumetric BMD as uncoupled quantities, by coupling these quantities by converting them to a single dual-energy X-ray absorptiometry (DXA) value. With this extension, the toolchain can also be evaluated using existing astronaut DXA data, which is important for evaluating its predictive ability for its intended purpose as a useful tool for spaceflight. While bed rest studies act as a spaceflight analog, it is unclear how well the model predicts volumetric BMD when individuals are exposed to additional factors like radiation and how model parameters need to change to account for these situations. Work on extending the toolchain in these areas is ongoing.

Appendix

TABLE 1.—BONE REMODELING MODEL PARAMETERS

Symbol	Value	Definition
D_{B_P}	7×10^{-4} pM day^{-1}	Differentiation rate of osteoblast progenitors
D_{B_r}	0.035 day^{-1}	Differentiation rate of responding osteoblasts
A_B	0.189 day^{-1}	Rate of elimination of active osteoblasts
D_{C_p}	0.0021 pM day^{-1}	Differentiation rate of osteoclast precursors
A_C	0.7 day^{-1}	Rate of osteoclast apoptosis caused by TGF-β
k_1	10^{-2} pM^{-1} day^{-1}	Rate of OPG-RANKL binding
k_2	10 day^{-1}	Rate of OPG-RANKL unbinding
k_3	5.8×10^{-4} pM^{-1}day^{-1}	Rate of RANK-RANKL binding
k_4	1.7×10^{-2} day^{-1}	Rate of RANK-RANKL unbinding
k_5	0.02 pM^{-1} day^{-1}	Rate of PTH binding with its receptor
k_6	3 day^{-1}	Rate of PTH unbinding
r_O	10×10^6 pmol day^{-1}/pmol cells	Rate of production of OPG per cell (rate adjusted due to change in modeling of anti-proliferation)
k_O	0.35 day^{-1}	Rate of elimination of OPG
r_L	10000 pM day^{-1}	Rate of RANKL production per pM B_r
k_L	50 day^{-1}	Rate of RANKL degradation
N_L	3×10^6 pmol/pmol cells	Maximum RANKL molecules attached to cell surface
K	10 pM	Fixed concentration of RANK
S_P	250 pm day^{-1}	Rate of synthesis of systemic PTH
k_P	86 day^{-1}	Rate of elimination of PTH
I_O	0 pM day^{-1}	Rate of administration of OPG
I_P	0 pM day^{-1}	Rate of administration of PTH
I_L	0 pM day^{-1}	Rate of administration of RANKL
T_B	8 pmol/g	TGF-β_1 concentration in bone
k_8/k_7	15.8 pM	TGF-β_1 dissociation constant
β	1/5 non dimensional	Hill factor for NO
G_D	0.37 non dimensional	PGE_2 constant related to dissociation
A_f^{cort}, A_r^{cort}	0.0275 mm^2	Cortical bone formation and resorption areas
A_f^{trab}, A_r^{trab}	0.0236 mm^2	Trabecular bone formation and resorption areas

References

Bassett, D. R., Wyatt, H. R., Thompson, H., Peters, J. C., and Hill, J. O. (2010). Pedometer-measured physical activity and health behaviors in U.S. adults. *Medicine & Science in Sports & Exercise*, 42(10):1819–1825.

Bergman, G. (2008). Orthoload. Charité Universitätsmedizin Berlin. http://www.OrthoLoad.com.

Bishop, C. M. (2006). *Pattern Recognition and Machine Learning*. Springer-Verlag, New York, Secaucus, NJ, USA.

Bonewald, L. F. (2006). Mechanosensation and transduction in osteocytes. *Bonekey Osteovision*, 3(10):7–15.

Bronner, F. and Worrell, R. V., editors (1999). *Orthopaedics: Principles of Basic and Clinical Science*. CRC Press, Boca Raton, FL, USA, 1st edition.

Carter, D. H., Fyhrie, D. P., and Whalen, R. T. (1987). Trabecular bone density and loading history: regulation of connective tissue biology by mechanical energy. *Journal of Biomechanics*, 20(8):785–794.

Cavanagh, P. R., Genc, K. O., Gopalakrishnan, R., Kulis, M. M., Maender, C. C., and Rice, A. J. (2010). Foot forces during typical days on the international space station. *Journal of Biomechanics*, 43(11):2182–2188.

Chang, K. L. and Pennline, J. A. (2013). Predicting bone mechanical state during recovery after long-duration skeletal unloading using QCT and finite element modeling. *NASA/TM-2013-217842*.

Cromwell, R. L. (2012). Human research program flight analogs project information package for bed rest studies. Technical report, National Aeronautics and Space Administration. Retrieved from https://www.nasa.gov/pdf/579501main_hrp_bed_rest_experiment_information_package.pdf.

Cromwell, R. L. (2013). Countermeasures and functional testing in head-down tilt bed rest (CFT 70). *JSC-CN-29943*.

Dean, C. M., Richards, C. L., and Malouin, F. (2001). Walking speed over 10 meters overestimates locomotor capacity after stroke. *Clinical Rehabilitation*, 15(4):415–421.

Eriksen, E. F. (2010). Cellular mechanisms of bone remodeling. *Reviews in Endocrine and Metabolic Disorders*, 11(4):219–227.

Fan, X., Roy, E., Zhu, L., Murphy, T. C., Ackert-Bicknell, C., Hart, C. M., Rosen, C., Nanes, M. S., and Rubin, J. (2004). Nitric oxide regulates receptor activator of nuclear factor-κb ligand and osteoprotegerin expression in bone marrow stromal cells. *Endocrinology*, 145(2):751–759.

Folkesson, J., Dam, E. B., Olsen, O. F., Pettersen, P. C., and Christiansen, C. (2007). Segmenting articular cartilage automatically using a voxel classification approach. *IEEE Transactions on Medical Imaging*, 26(1):106–115.

Frost, H. M. (2003). Bone's mechanostat: A 2003 update. *Anatomical Record Part A: Discoveries in Molecular, Cellular, and Evolutionary Biology*, 275A(2):1081–1101.

Genc, K. O., Humphreys, B. T., and Cavanagh, P. R. (2009). Enhanced daily load stimulus to bone in spaceflight and on earth. *Aviation, Space, and Environmental Medicine*, 80(11):919–926.

Gere, J. M. (2004). *Mechanics of Materials*. Thomson Brooks/Cole, Belmont, CA, USA, 6th edition.

Giambini, H., Dragomir-Daescu, D., Nassr, A., Yaszemski, M. J., and Zhao, C. (2014). Quantitative computed tomography protocols affect material mapping and quantitative computed tomography-based finite-element analysis predicted stiffness. *Journal of Biomechanical Engineering*, 48(1):153–161.

Goodship, A. E., Cunningham, J. L., Oganov, V., Darling, J., Miles, A. W., and Owen, G. W. (1998). Bone loss during long term space flight is prevented by the application of a short term impulsive mechanical stimulus. *Acta Astronautica*, 43(3-6):65–75.

Hansen, N. (2006). The CMA evolution strategy: a comparing review. In Lozano, J. A., Larrañaga, P., Inza, I., and Bengoetxea, E., editors, *Towards a New Evolutionary Computation: Advances in the Estimation of Distribution Algorithms*, pages 75–102. Springer, Berlin, Heidelberg.

Hazelwood, S. J. and Castillo, A. B. (2007). Simulated effects of marathon training on bone density, remodeling, and microdamage accumulation of the femur. *International Journal of Fatigue*, 29(6):1057–1064.

Hazelwood, S. J., Martin, R. B., Rashid, M. M., and Rodrigo, J. J. (2001). A mechanistic model for internal bone remodeling exhibits different dynamic responses in disuse and overload. *Journal of Biomechanics*, 34(3):299–308.

Hering, S., Isken, F., Knabbe, C., Janott, J., Jost, C., Pommer, A., Muhr, G., Schatz, H., and Pfeiffer, A. F. H. (2010). TGFβ1 and TGFβ2 mRNA and protein expression in human bone samples. *Experimental and Clinical Endocrinology & Diabetes*, 109(1):217–226.

Hernandez, C. J., Beaupré, G. S., Keller, T. S., and Carter, D. R. (2001). The influence of bone volume fraction and ash fraction on bone strength and modulus. *Bone*, 29(1):74–78.

Hernandez, C. J., Hazelwood, S. J., and Martin, R. B. (1999). The relationship between basic multicellular unit activation and origination in cancellous bone. *Bone*, 25(5):585–587.

Hooke, R. (1678). *Lectures de potentia restitutiva, or of spring. Explaining the power of springing bodies.* John Martyn, London, 1st edition.

Janssens, K., ten Dijke, P., Janssens, S., and Van Hul, W. (2005). Transforming growth factor-β1 to the bone. *Endocrine Reviews*, 26(6):743–774.

Jilka, R. L., Weinstein, R. S., Bellido, T., Roberson, P., Parfitt, M., and Manolagas, S. C. (1999). Increased bone formation by prevention of osteoblast apoptosis with parathyroid hormone. *Journal of Clinical Investigation*, 104(4):439–446.

John, G. H. and Langley, P. (1995). Estimating continuous distributions in bayesian classifiers. *Proceedings of the Eleventh Conference on Uncertainty in Artificial Intelligence*, pages 338–345.

Kaneko, T. S., Bell, J. S., Pejcic, M. R., Tehranzadeh, J., and Keyak, J. H. (2004). Mechanical properties, density and quantitative CT scan data of trabecular bone with and without metastases. *Journal of Biomechanics*, 37(4):523–530.

Kaneko, T. S., Pejcic, M. R., Tehranzadeh, J., and Keyak, J. H. (2003). Relationships between material properties and CT scan data of cortical bone with and without metastatic lesions. *Medical Engineering and Physics*, 26(4):445–454.

Keyak, J. H., Kaneko, T. S., Tehranzadeh, J., and Skinner, H. B. (2005). Predicting proximal femoral strength using structural engineering models. *Clinical Orthopaedics and Related Research*, 437:219–228.

Keyak, J. H., Lee, I. Y., and Skinner, H. B. (1994). Correlations between orthogonal mechanical properties and density of trabecular bone: Use of different densiometric measures. *Journal of Biomedical Materials Research*, 28(11):1329–1336.

Kim, S. J., Yang, W. G., Cho, E., and Park, E. C. (2012). Relationship between weight, body mass index and bone mineral density of the lumbar spine in women. *Journal of Bone Metabolism*, 19(2):95–102.

Lang, T., LeBlanc, A. D., Evans, H. J., and Lu, Y. (2006). Adaptation of the proximal femur to skeletal reloading after long-duration spaceflight. *Journal of Bone and Mineral Research*, 21(8):1224–1230.

Lang, T., LeBlanc, A. D., Evans, H. J., Lu, Y., Genant, H., and Yu, A. (2004). Cortical and trabecular bone mineral loss from the spine and hip in long-duration spaceflight. *Journal of Bone and Mineral Research*, 19(6):1006–1012.

LeBlanc, A. D., Spector, E. R., Evans, H. J., and Sibonga, J. D. (2007). Skeletal responses to space flight and the best rest analog: a review. *Journal of Musculoskeletal and Neuronal Interactions*, 7(1):33–47.

Lemaire, V., Tobin, F. L., Greller, L. D., Cho, C. R., and Suva, L. J. (2004). Modeling the interactions between osteoblast and osteoclast activities in bone remodeling. *Journal of Theoretical Biology*, 229(3):293–309.

Malan, D. F., Botha, C. P., and Valstar, E. R. (2013). Voxel classification and graph cuts for automated segmentation of pathological periprosthetic hip anatomy. *International Journal of Computer Assisted Radiology and Surgery*, 8(1):63–74.

Mitchell, T. M. (1997). *Machine Learning*. McGraw-Hill, Inc., New York, NY, USA, 1 edition.

Naganathan, V. and Sambrook, P. (2003). Gender differences in volumetric bone density: a study of opposite-sex twins. *Osteoporosis International*, 14(7):564–569.

Nelson, E. S., Lewandowski, B. E., Licata, A., and Myers, J. G. (2009). Development and validation of a predictive bone fracture risk model for astronauts. *Annals of Biomedical Engineering*, 37(11):2337–2359.

Orwoll, E. S., Adler, R. A., Amin, S., Binkley, N., Lewiecki, E. M., Petak, S. M., Shapses, S. A., Mehrsheed, S., Watts, N. B., and Sibonga, J. D. (2013). Skeletal health in long-duration astronauts: nature, assessment, and management recommendations from the NASA bone summit. *Journal of Bone and Mineral Research*, 28(6):1243–1255.

Ott, S. M. (2010). Bone physiology. University of Washington. https://courses.washington.edu/bonephys/physiology.html.

Parfitt, A. (1988). Bone remodeling: relationship to the amount and structure of bone, and the pathogenesis and prevention of fractures. In Riggs, B. L. and Melton III, J. L., editors, *Osteoporosis: Etiology, Diagnosis, and Management*, pages 45–93. Raven Press, New York, NY, USA, 1st edition.

Pennline, J. A. (2009). Simulating bone loss in microgravity using mathematical formulations of bone remodeling. *NASA/TM-2009-215824*.

Pennline, J. A. and Mulugeta, L. (2014a). A computational model for simulating spaceflight induced bone remodeling. In *Proceedings of the 44th International Conference on Environmental Systems*, Tucson, Arizona, 2014.

Pennline, J. A. and Mulugeta, L. (2014b). Evaluating daily load stimulus formulas in relating bone response to exercise. *NASA/TM-2014-218306*.

Pennline, J. A. and Mulugeta, L. (2017). Mapping bone mineral density obtained by quantitative computed tomography to bone volume fraction. *NASA/TM-2017-219490*.

Pfeilschifter, J., Diel, I., Scheppach, B., Bretz, A., Krempien, R., Erdmann, J., Schmid, G., Reske, N., Bismar, H., Seck, T., Krempien, B., and Ziegler, R.

(1998). Concentration of transforming growth factor beta in human bone tissue: relationship to age, menopause, bone turnover, and bone volume. *Journal of Bone and Mineral Research*, 13(4):716–730.

Pivonka, P., Zimak, J., Smith, D. W., Gardiner, B. S., Dunstan, C. R., Sims, N. A., Martin, T. J., and Mundy, G. R. (2008). Model structure and control of bone remodeling: a theoretical study. *Bone*, 43(2):249–263.

Ploutz-Snyder, L. L., Downs, M., Ryder, J., Hackney, K., Scott, J., Buxton, R., Goetchius, E., and Crowell, B. (2014). Integrated resistance and aerobic exercise protects fitness during bed rest. *Medicine & Science in Sports & Exercise*, 46(2):358–368.

Raz, A. (1972). Interaction of prostaglandins with blood plasma proteins. comparative binding of prostaglandins A_2, $F_{2\alpha}$ and E_2 to human plasma proteins. *Biochemical Journal*, 130(2):631–636.

Riggs, B. L., Melton, L. J., Robb, R. A., Camp, J. J., Atkinson, E. J., Peterson, J. M., Rouleau, P. A., McCollough, C. H., Bouxsein, M. L., and Khosla, S. (2004). Population-based study of age and sex differences in bone volumetric density, size, geometry, and structure at different skeletal sites. *Journal of Bone and Mineral Research*, 19(12):1945–1954.

Roodman, G. D. (1999). Cell biology of the osteoclast. *Experimental Hematology*, 27(8):1229–1241.

Shackelford, L. C., LeBlanc, A. D., Driscoll, T. B., Evans, H. J., Rianon, N. J., Smith, S. M., Spector, E., Feeback, D. L., and Lai, D. (2004). Resistance exercise as a countermeasure to disuse-induced bone loss. *Journal of Applied Physiology*, 97(1):119–129.

Sibonga, J. D., Cavanagh, P. R., Lang, T. F., LeBlanc, A. D., Schneider, V. S., Shackelford, L. C., Smith, S. M., and Vico, L. (2007a). Adaptation of the skeletal system during long-duration spaceflight. *Clinical Reviews in Bone and Mineral Metabolism*, 5(4):249–261.

Sibonga, J. D., Evans, H. J., Smith, S. A., Spector, E. R., Yardley, G., and Myers, J. (2017). Evidence report: risk of bone fracture due to spaceflight-induced changes to bone. *JSC-CN-39591*.

Sibonga, J. D., Evans, H. J., Sung, H. G., Lang, T. F., Organov, V. S., Bakulin, A. V., Shackelford, L. C., and LeBlanc, A. D. (2007b). Recovery of spaceflight-induced bone loss: bone mineral density after long duration missions as fitted with an exponential function. *Bone*, 41(6):973–978.

Smith, S. M., Heer, M. A., Shackelford, L. C., Sibonga, J. D., Ploutz-Snyder, L. L., and Zwart, S. R. (2012). Benefits for bone from resistance exercise and nutrition in long-duration spaceflight: evidence from biochemistry and densitometry. *Journal of Bone and Mineral Research*, 27(9):1896–1906.

Taibbi, G., Cromwell, R. L., Zanello, S. B., Yarbough, P. O., Ploutz-Snyder, R. J., Godley, B. F., and Vizzeri, G. (2016). Ocular outcomes comparison between 14- and 70-day head-down-tilt bed rest. *Investigative Ophthalmology and Visual Science*, 57(2):495–501.

Tripathi, R. C., Borisuth, N. S., Kolli, S. P., and Tripathi, B. J. (1993). Trabecular cells express receptors that bind TGF-beta 1 and TGF-beta 2: a qualitative and quantitative characterization. *Investigative Ophthalmology & Visual Science*, 34(1):260–263.

Turner, C. H. and Robling, A. G. (2003). Designing exercise regiments to increase bone strength. *Exercise and Sport Sciences Reviews*, 31(1):45–50.

van Loon, J. J. W. A., Veldhuijzen, J. P., and Burger, E. H. (1996). *Bone and space flight: an overview*, pages 259–299. Springer Berlin Heidelberg.

Vico, L., Collet, P., Guignandon, A., Lafage-Proust, M. H., Thomas, T., Rehaillia, M., and Alexandre, C. (2000). Effects of long-term microgravity exposure on cancellous and cortical weight-bearing bones of cosmonauts. *Lancet*, 355(9215):1607–1611.

Wang, S. and Summers, R. M. (2012). Machine learning and radiology. *Medical Image Analysis*, 16(5):933–951.

Werner, C. R. and Gorla, R. S. R. (2013). Probabilistic study of bone remodeling using finite element analysis. *International Journal of Applied Mechanics and Engineering*, 18(3):911–921.

Whalen, R. T., Carter, D. R., and Steele, C. R. (1988). Influence of physical activity on the regulation of bone density. *Journal of Biomechanics*, 21(10):825–837.

White, R. J. and McPhee, J. C. (2007). The digital astronaut: an integrated modeling and database system for space biomedical research and operations. *Acta Astronautica*, 60(4):273–280.

Zérath, E. (1998). Effects of microgravity on bone and calcium homeostasis. *Advances in Space Research*, 21(8-9):1049–1058.

Zumsande, M., Stiefs, D., Siegmund, S., and Gross, T. (2011). General analysis of mathematical models for bone remodeling. *Bone*, 48(4):910–917.